Ultrasound in Med. & Biol., Vol. 34, No. 6, pp. 981–1000, 2008

0301-5629/08/$–see front matter

ELSEVIER

doi:10.1016/j.ultrasmedbio.2007.11.012

● *Original Contribution*

SPACE VARIANT ULTRASOUND FREQUENCY COMPOUNDING BASED ON NOISE CHARACTERISTICS

YAEL EREZ,* YOAV Y. SCHECHNER,† and DAN ADAM‡

*IBM Haifa Research Lab, Haifa, Israel; †Dept. of Electrical Engineering, Technion - Israel Institute of Technology, Haifa, Israel; and ‡Dept. of Biomedical Engineering, Technion - Israel Institute of Technology, Haifa, Israel

(*Received* 30 *December* 2006; *revised* 7 *October* 2007; *in final form* 14 *November* 2007)

Abstract—Ultrasound images are very noisy. Along with system noise, a significant noise source is the speckle phenomenon caused by interference in the viewed object. Most of the past approaches for denoising ultrasound images essentially blur the image and they do not handle attenuation. We discuss an approach that does not blur the image and handles attenuation. It is based on frequency compounding, in which images of the same object are acquired in different acoustic frequencies and, then, compounded. Existing frequency compounding methods have been based on simple averaging, and have achieved only limited enhancement. The reason is that the statistical and physical characteristics of the signal and noise vary with depth, and the noise is correlated between acoustic frequencies. Hence, we suggest two spatially varying frequency compounding methods, based on the understanding of these characteristics. As demonstrated in experiments, the proposed approaches suppress various noise sources and also recover attenuated objects while maintaining a high resolution. (E-mail: yaele@il.ibm.com)

Key Words: **Frequency compounding, Image processing.**

INTRODUCTION AND LITERATURE

Ultrasound is an imaging technique that uses high frequency acoustic waves (Meire and Farrant 1995). It is safe, suitable for many applications and is relatively affordable. It is used in sonar, medical imaging and material science work. However, there are problems that interfere with diagnosis based on such images. Figure 1 illustrates some of these problems. The most prominent one, which distinguishes ultrasound from most imaging techniques, is the strong speckle noise. Speckles appear as grains of different sizes and intensities that result from the coherent nature of the ultrasound radiation (Angelsen 2000; Webb 1988). The speckle image is signal dependent. It is time invariant and, thus, cannot be suppressed by temporal averaging. A second problem is attenuation. The acoustic signal propagating in the medium is scattered and absorbed (Angelsen 2000) and, hence, attenuated. This phenomenon is more pronounced in high acoustic frequencies. When the attenuated signal is amplified, it is accompanied by the amplification of system noise, which is signal independent. Below a certain level of signal-to-noise ratio (SNR), objects are overwhelmed by system noise, thus, amplification in postprocessing inhibits reconstruction of these objects.

Most of the past approaches for denoising ultrasound images have used standard image enhancement tools, such as weighted median filter (Loupas et al. 1989), wavelet based methods (Cincotti et al. 2001; Gupta et al. 2004), Gaussian non-linear filters (Aurich and Weule 1995) and anisotropic diffusion (Weickert 1997). All these methods essentially blur the image. Moreover, most of them do not handle spatially varying physical effects, such as attenuation. It is worth noting, that some studies based on a single frequency band spatially adapt the denoising filter (Busse et al. 1995). Another approach is *compounding,* in which images of an object are acquired in different conditions, and then compounded (Burckhardt 1978; Magnin et al. 1982). Common compounding methods are spatial compounding and frequency compounding. In spatial compounding, images of the same region are acquired from different viewpoints. The change of viewpoint induces a complex registration problem, since the object is three dimensional while only a two-dimensional (2D) slice is seen. In frequency compounding, the frames are acquired in different acoustic frequencies. Existing compounding methods (Amir et al. 1986) have used simple processing

Address correspondence to: Yael Erez, IBM Haifa Research Lab, Mount Carmel, Haifa 31905, Israel. E-mail: yaele@il.ibm.com

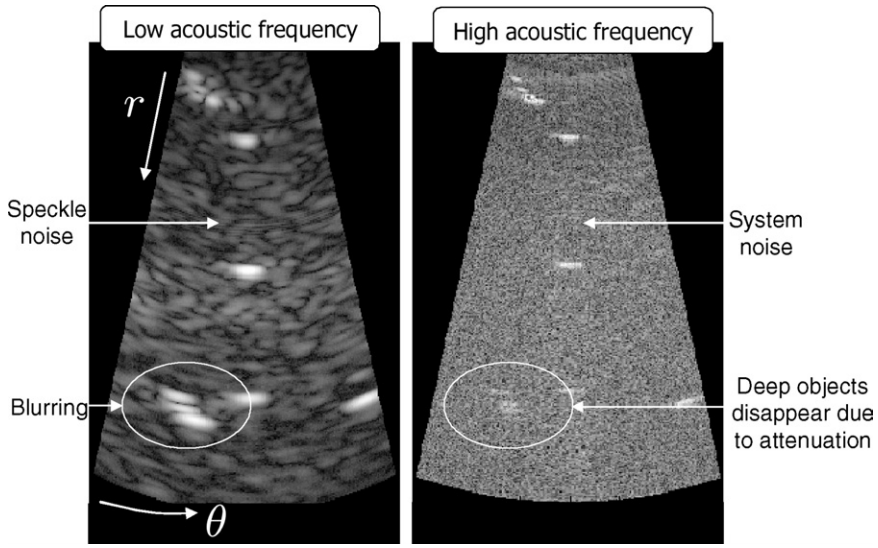

Fig. 1. Problems that disrupt interpretations of ultrasound images. The depth range is 0–12 *cm.*

methods such as point-wise arithmetic averaging and have achieved only limited enhancement.

In this article, we present two new methods that are based on frequency compounding: depth-dependent averaging and stocahstic reconstruction. Both methods are spatially varying and they are based on physical characteristics of the signal and noise as a function of depth and acoustic frequency (AF). The depth-dependent averaging reconstructs deep objects and bypasses resolution loss. It can easily be performed on the fly. The stochastic denoising is based on understanding of noise statistics. Hence, we compare current models of noise statistics with empirical noise estimation. We show that the current models do not match the real measurements well. Thus, we explore the statistics based on empirical estimations. The stochastic reconstruction shows significant speckle reduction, with no apparent resolution loss, while deep objects are reconstructed too. Partial preliminary results appeared in (Erez et al. 2006).

In the following parts of this section, we define the variables used in this article and briefly overview the relevant models of image formation and noise models from the literature. In subsequent sections, we describe the mathematical methods we use for image analysis, as well as experiments.

Image formation

Consider ultrasound images as 2D fields, given in polar coordinates (r, θ). The r coordinate (radial axis) is the axis of wave propagation, and θ (lateral axis) represents a serial scan of the direction of the radiating ultrasound beam. The 2D signal measured by the system is the result of natural filtering of the volumetric object

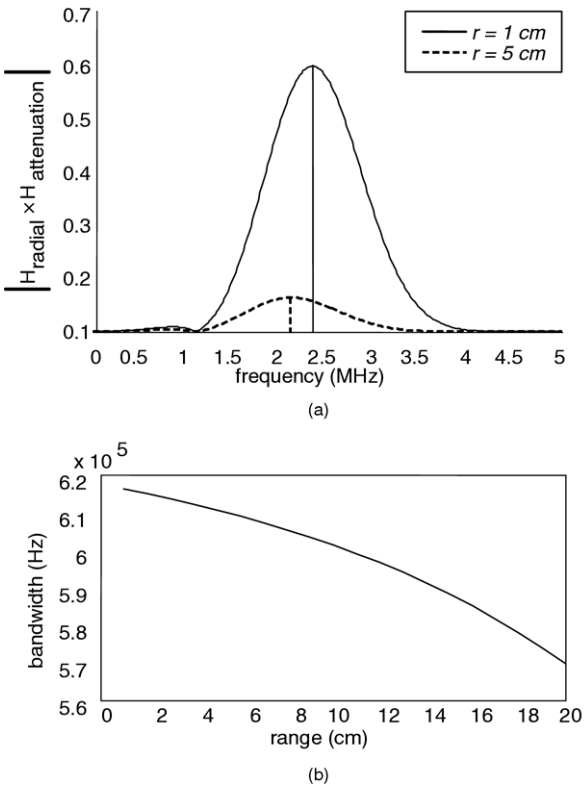

Fig. 2. Attenuation phenomena. (a) Absolute value of the radial transfer function for different distances from the probe. The farther the probe is from the measurement point, the lower is the dominant AF. (b) Bandwidth at different distances from the probe. The farther the probe is from the measurement point, the narrower the band is.

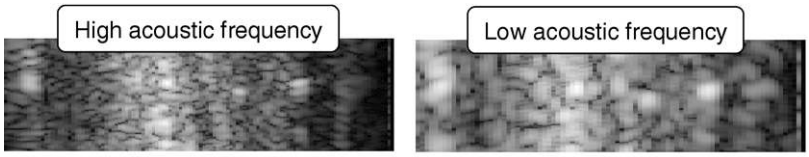

Fig. 3. Speckle appearance of the same tissue in different AFs. High AF speckles (a) are smaller than the low AF speckles (b).

reflectivity function $a_0(r,\ \theta)$ with a 2D point spread function (PSF). This PSF is space variant. In particular, its lateral support changes with the depth *r:* the acoustic beam is focused at a certain depth, where the lateral PSF is narrowest, while at other depths this PSF gradually widens. Yet, in small regions we can assume this filter to be space invariant. There, the measured signal, accounting for blur, is

$$a^{\mathrm{RF}}(r,\theta) = a_0(r,\theta) * h(r,\theta), \tag{1}$$

where $h(r,\ \theta)$ is the PSF, disregarding attenuation. Following (Wagner et al, 1983), it is reasonable to assume the PSF to be separable. The PSF also depends on the system properties (such as the relation between AF and resolution (Angelsen 2000)) and somewhat also on the tissue properties (Angelsen 2000).

Image formation is also affected by attenuation of ultrasound in the medium (Angelsen 2000; Kristoffersen et al. 1998). A general simple and effective model of the amplitude of the signal is

$$a^{\mathrm{RF}}(r,\theta) = e^{-2\alpha r f_{\mathrm{acoustic}}} a_0(r,\theta) * h(r,\theta), \tag{2}$$

where α is the *attenuation coefficient* of the acoustic amplitude, and f_{acoustic} is the AF. A rule of thumb (Angelsen 2000) is: attenuation in tissue is approximately $1dB/(cm \cdot MHz)$, for a signal going from a probe to the object and then returning. It is clear from eqn. 2 that attenuation depends on the AF: high AFs suffer from stronger attenuation and thus a lower SNR, particularly at large depths. This is evident in Fig. 1.

Note that the dependency of the attenuation on the AF changes the acoustic spectrum of the signal. Figure 2 presents the Fourier envelope of a temporal signal, as it is multiplied by an exponential attenuation. The plot illustrates this product near the probe (1 *cm*) and far from it (5 *cm*). It also represents the bandwidth at different depths. The farther the probe is from the measurement point, the lower is the dominant AF, and the narrower is the acoustic band.

In ultrasound systems, the measured signal a^{RF} undergoes several standard conversion steps. First, attenuation is compensated for. Then, the acoustic modulation is extracted: note that a^{RF} is a high-frequency (*MHz*) signal, which is modulated by the tissue reflectivity function. To extract the tissue information, the envelope of the attenuation-compensated a^{RF} is detected (Oppenheim and Schafer 1975), yielding

$$a^{\mathrm{envelope}}(r,\theta) = \mathrm{envelope}[e^{2\alpha r f_{\mathrm{acoustic}}} \cdot a^{\mathrm{RF}}(r,\theta)], \tag{3}$$

where envelope $[g(r)]$ is an operator (Angelsen, 2000) that extracts the envelope of a modulated wave $g(r)$. The envelope is complex, in general, yet the operation

$$a^{\mathrm{magnitude}}(r,\theta) = \left| a^{\mathrm{envelope}}(r,\theta) \right| \tag{4}$$

derives its *modulus.*

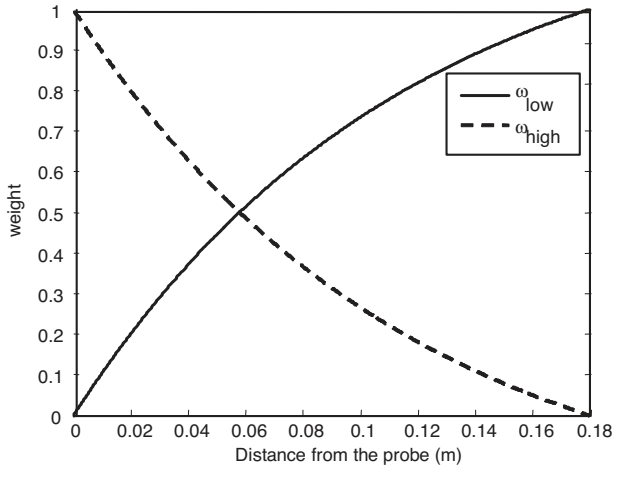

Fig. 4. An example for weight functions, with $r_{\mathrm{equilibrium}} = 6$ *cm.*

Speckle noise

Speckle noise has a granular texture, as presented in Fig. 3. Speckles degrade the ability to resolve details and

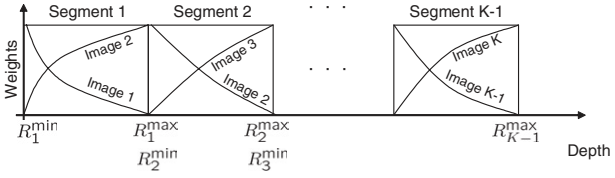

Fig. 5. Depth-dependent averaging for K images.

detect objects with a size comparable to their own. They stem from point scatterers that cannot be resolved by the ultrasound system. These point scatterers, which are smaller than the ultrasound wavelength, may be very close to one another. Two or more waves travelling to the probe from such scatterers may interfere with each other, constructively or destructively, creating bright and dark spots, termed speckles. For interference, the backscattered signal from the scatterers should overlap in time and space. This happens when the distance between them is within the PSF (radially and laterally) support. This is an important point to remember: the speckle typical size is similar to the PSF support. Since the PSF changes with depth, the statistics of this noise source are space (depth)-variant. Furthermore, they change when the AF used to acquire the image changes, as shown in Fig. 3, as does the PSF. In this article, we exploit these properties.

Speckle is generally modelled as multiplicative noise (Jain 1989). The overall detected magnitude is

$$a^{\text{total}}(r,\theta) = a^{\text{magnitude}}(r,\theta)\cdot s^{\text{magnitude}}(r,\theta) + \eta(r,\theta), \quad (5)$$

where the real number $s^{\text{magnitude}}$ represents nonnegative speckle noise at a certain coordinate and η represents the system noise there. The system noise increases with depth, due to the attenuation compensation done in eqn 3. Still, assume for a moment that the additive noise is sufficiently small compared to the multiplicative noise. Then, a log operation on eqn 5 transforms speckles to additive noise

$$\underbrace{\log\left(a^{\text{total}}\right)}_{a^{\log}} \approx \underbrace{\log\left(a^{\text{magnitude}}\right)}_{\log\left(a^{\text{magnitude}}\right)} + \underbrace{\log\left(s^{\text{magnitude}}\right)}_{s^{\log}}. \quad (6)$$

We note that the logarithm operation is standard for displaying ultrasound images on a computer screen (Angelsen 2000), since the dynamic range of a^{total} is very large (Angelsen 2000), thus the logarithm enables image display. Therefore, in the image used for display, the speckle noise is already additive.

Prior models for noise statistics

It is common to model the additive noise in eqn 6 as white (Abd-Elmoniem et al. 2002) or stationary (Cincotti et al. 2001), although neither is true. There are, however, more accurate models. Here we survey prior models drawn from the literature of ultrasound (Angelsen 2000) as well as of optics (Goodman 1995), image processing (Jain 1989) and laser (Dainty 1975) (Note that optical detectors measure the average intensity during the exposure time, and not the phase. In contrast, an ultrasonic detector can detect the time varying complex amplitude. Hence, the information it yields about speckles is richer and one can notice interference phenomena even when the signal is wideband). We mainly deal here with statistics that characterize media with an homogenous distribution of small scatterers.

Wagner et al. (1983) showed that under several assumptions, the auto-correlation of the speckle envelope is

$$R^{\text{envelope}}(\Delta r,\Delta\theta) \approx \left|a_s\right|^2 h(-\Delta r,-\Delta\theta) * h^*(\Delta r,\Delta\theta), \quad (7)$$

where $(\Delta r, \Delta\theta)$ is the lag between image points and a_s is a constant that depends on the viewed object. Wagner et al. (1983) also used the separability property of the PSF to write the auto-correlation as a product of radial and angular auto-correlations:

$$R^{\text{envelope}}(\Delta r,\Delta\theta) \approx R^{\text{envelope}}_{\text{radial}}(\Delta r)\cdot R^{\text{envelope}}_{\text{lateral}}(\Delta\theta), \quad (8)$$

Assuming the PSF to be an even function, Wagner et al. (1983) derived the speckle *magnitude* auto-correlation

$$R^{\text{magnitude}}(\Delta r,\Delta\theta) = (\kappa_2)({}_2F_1)\left(-\frac{1}{2},-\frac{1}{2};1;\left|\frac{R^{\text{envelope}}(\Delta r,\Delta\theta)}{R^{\text{envelope}}(0,0)}\right|^2\right), \quad (9)$$

where κ_2 is a normalization factor and $({}_2F_1)$ is Gauss's hypergeometric function.

In frequency compounding, images of the same scene are acquired in different PSFs. This brings up a question: what is the cross-correlation between corresponding pixels in such images? Walker and Trahey (1998) computed the cross-correlation between images acquired by different imaging systems. They showed that the cross-correlation coefficient of speckle envelopes is

$$\rho^{\text{envelope}} = \left(\frac{\int_{-\infty}^{\infty} H_1(f_t)H_2^*(f_t)df_t}{\sqrt{\int_{-\infty}^{\infty}\left|H_1(f_t)\right|^2 df_t \int_{-\infty}^{\infty}\left|H_2(f_t)\right|^2 df_t}}\right)^2, \quad (10)$$

where H_1 and H_2 are the transfer functions of the systems. From eqn 10, the cross-correlation between the speckle envelopes is computed as the square of the cross-correlation coefficient between the transfer functions that are used for signal acquisition. Hence, the cross-correlation coefficient depends on the overlap of the Fourier transforms of the PSFs. This result applies only to corresponding pixels. A more general model should include lag between pixels, *i.e.,* $\Delta r \neq 0$ and $\Delta\theta \neq 0$.

MATERIALS AND METHODS

Experimental set-up

We conducted experiments using a commercial medical ultrasonic system, the GE Vivid 3. The electronic signal

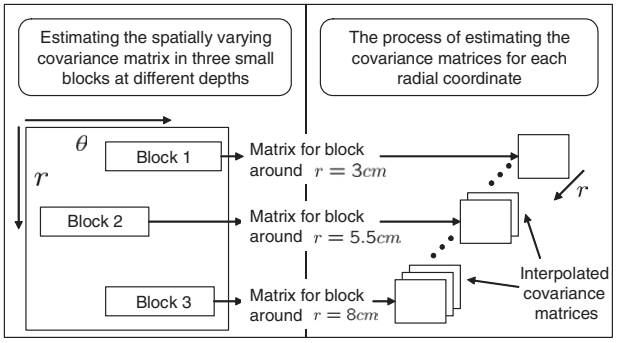

Fig. 6. Estimating the spatially varying covariance matrix.

generated by this system is a square burst with duration of three half periods. The probes used are phased arrays named 3s and 5s (by GE Medical Systems, Milwaukee, WI, USA). The data was obtained from a tissue-mimicking phantom, for controlled and repeatable setups. Fat was placed on top of the phantom to demonstrate an attenuating layer. Different AFs were used to acquire images. We have direct access to a^{RF}, received in MHz from the medium. From here, we directly apply sampling, attenuation compensation, envelope detection and magnitude to produce $a^{magnitude}$ and, then, a log operation yields a^{log}.

Estimation of noise statistics

In a previous section, prior models of noise statistics in ultrasound images were detailed. We wish to compare these models with empirical measurements. The noise consists of speckle noise as well as system noise. We estimate the noise within areas that have no strong reflectors. Therefore, the area is dominated by the two noise sources. When empirically estimating the noise statistics, it is important to note that speckle statistics vary radially since the PSF changes with the distance from the transducer. +We, thus, apply empirical analysis to small blocks. In addition, radial and lateral correlations differ. In the radial direction, the signals s_k and s_i acquired in different AFs are one dimensional. Their estimated cross-correlation (Papoulis 1965) is

$$\hat{R}^{radial}_{s_k s_i}(\Delta r) = \frac{1}{L-\Delta r}\sum_{l=0}^{L-\Delta r-1}\{S_k[l] - \hat{\mu}_{s_k}\}\{S_i[l+\Delta r] - \hat{\mu}_{s_k}\}, 0 \le \Delta r < L, \quad (11)$$

where Δr is the radial lag between pixels, $\hat{\mu}_s$ is the estimated mean of a signal s, and L is the number of samples in the radial segment. To increase the reliability of this estimation we averaged its value over a range of θ in a 2D block. When $k = i$, eqn 11 degenerates to an auto-correlation estimate

$$\hat{R}^{\text{radial}}_{s_k}(\Delta r) = \frac{1}{L-\Delta r}\sum_{l=0}^{L-\Delta r-1}\{S_k[l] - \hat{\mu}_{s_k}\}\cdot \{s_k[l+\Delta r] - \hat{\mu}_{s_k}\}, \quad 0 \le \Delta r < L. \quad (12)$$

The correlation in the lateral direction $\hat{R}^{\text{lateral}}_{s_k s_i}(\Delta\theta)$ is estimated in a very similar way, where the lag between pixels is in the lateral direction, rather than in the radial one.

In the Empirical noise statistics section, we explore the auto-correlation and the cross-correlation both in the radial and lateral directions. For each of these cases, we compare the prior models [eqns. 9 and 10] with empirical noise measurements. For the auto-correlation, the comparison is made regarding $a^{magnitude}$ (eqn 4). For cross-correlation, the comparison is made regarding $a^{envelope}$ (eqn 3), since the model in the literature (Walker and Trahey 1998) exists for the envelope signal. In all the theoretical calculations made for the comparisons, we factored the attenuation $e^{-2\alpha r f_{acoustic}}$ (eqn 2) into the PSF, when using it in eqns 9 and 10. We study empirically the measurements made in various AFs and various distances, in order to observe their influence on the correlation functions.

Depth-dependent averaging

We now present our first frequency compounding method. It is space variant and we term it *depth-dependent averaging*. It is motivated by some physical principles characterizing images acquired with different AFs. Attenuation is different when using different AFs (eqn 2). Hence, for a fixed distance from the probe, noise can change from speckle in a low AF image, to system noise in a high AF image. Furthermore, a high AF image has a better resolution but may suffer from a lower signal-to-system-noise ratio. Usually, near the probe, where attenuation is negligible, we should prefer to use high AFs, while far from the probe, where attenuation is high, we should prefer to use low AFs.

On one hand, the method should overcome system noise, in order to reconstruct deep objects. On the other hand, we aim to avoid loss of resolution associated with low AFs, when reconstructing objects closer to the transducer. Compounding by a depth-dependent averaging is, thus, suggested here. Near the probe, more weight is given to the high AF images. Far from the probe, more weight is given to the low AF images. In this way, high

Table 1. A reference to the noise statistics analysis.

	Radial	Lateral
Auto-correlation	Sec. III-A.1	Sec. III-A.2
Cross-correlation	Sec. III-A.3	Sec. III-A.3

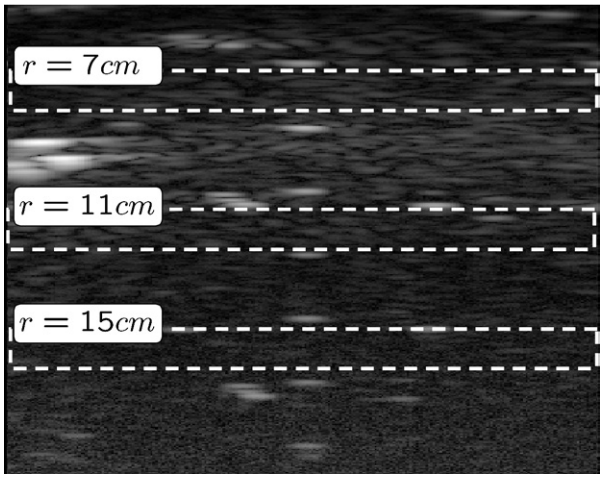

Fig. 7. Regions in which the radial correlation functions are estimated.

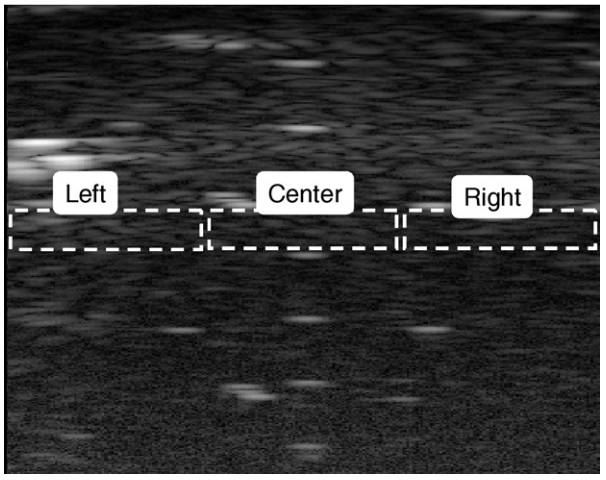

Fig. 8. Regions in which the lateral correlation functions are estimated. All regions are at a radial distance of 11 *cm.*

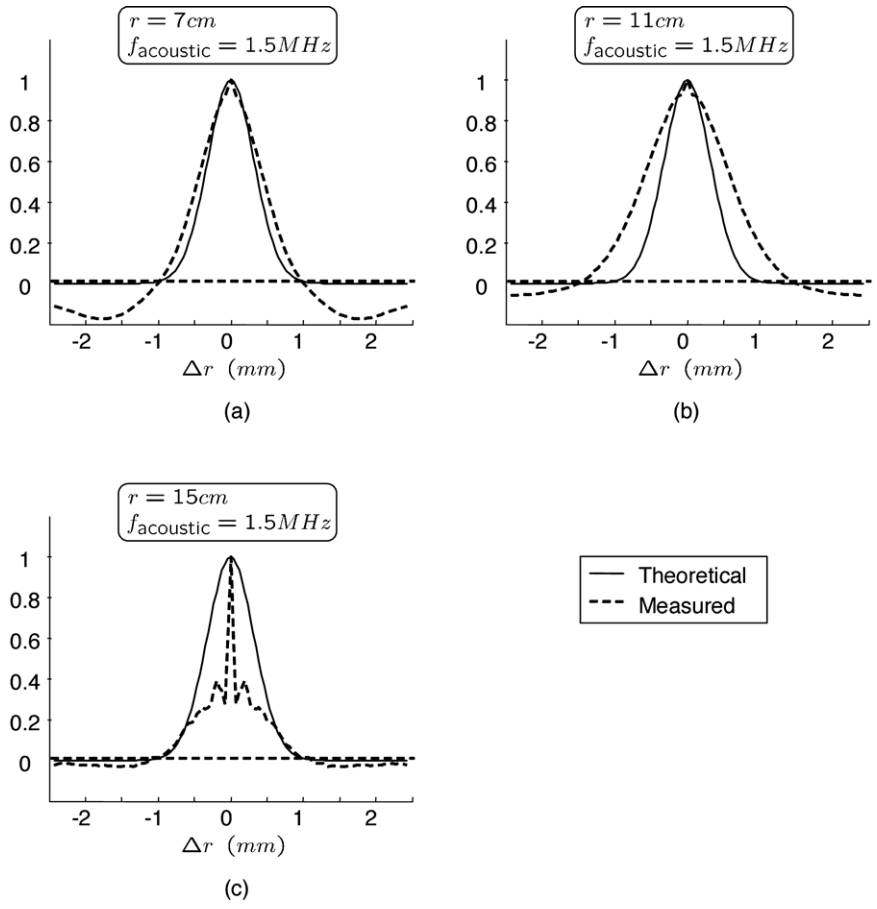

Fig. 9. Theoretical radial normalized auto-correlation, compared to the estimation, at various radial distances. The model is similar to the estimation near the probe (a), and is incorrect at other radial distances (b) and (c).

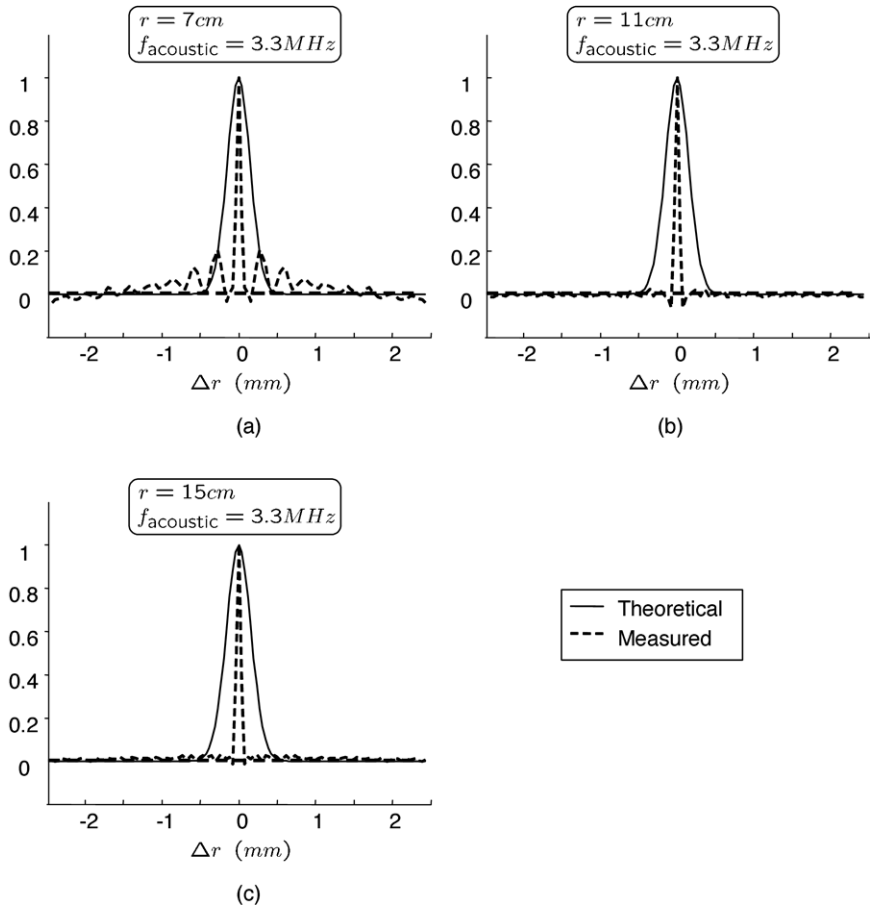

Fig. 10. Theoretical radial normalized auto-correlation, compared to the estimation, at various radial distances. Here $f_{\text{acoustic}} = 3.3\ MHz$. The model is incorrect at all radial distance.

resolution is obtained near the probe, and a high ratio of signal to system-noise is maintained far from the probe.

Compounding two frequencies

When weighting two images, the question is how to choose the weights? Let $\omega_{\text{high}}(r)$ be a weight function for the high AF image. Then we set $\omega_{\text{low}}(r) = 1 - \omega_{\text{high}}(r)$ as the weight of the low AF image. The weights may satisfy

$$\omega_{\text{high}}(0) = 1 \tag{13}$$

$$\omega_{\text{high}}(R_{\max}) = 0, \tag{14}$$

where $R_{\max}$ is the maximum depth in the compounded image. Equation 13 enables us to use only the high AF image near the probe. As stated, near the probe the high AF image presents no significant attenuation, and has a better radial resolution. Equation 14 enables us to use only the low AF image far from the probe, to maintain a high signal to system-noise ratio.

For example, we used

$$\omega_{\text{high}}(r) = \frac{e^{-\alpha_{\text{high}} r} - e^{-\alpha_{\text{high}} R_{\max}}}{1 - e^{-\alpha_{\text{high}} R_{\max}}}, \tag{15}$$

The corresponding weights are plotted in Fig. 4. The parameters α_{high} and $r_{\text{equilibrium}}$ will be explained later. These weights are not a result of a mathematical analysis, yet they have the following characteristics:

- The weight ω_{high} is related to r in an exponential way. This is motivated by the exponential relation between depth and attenuation presented in eqn 2.
- The parameter $r_{\text{equilibrium}}$ is the depth where $\omega_{\text{high}}(r) = \omega_{\text{low}}(r)$. It can be set by the user. By default, one can assign $r_{\text{equilibrium}} = \dfrac{R_{\max}}{2}$.
- The parameter α_{high} controls the exponential-rate. It is related to $r_{\text{equilibrium}}$. For a given $r_{\text{equilibrium}}$ one can find α_{high} which satisfies

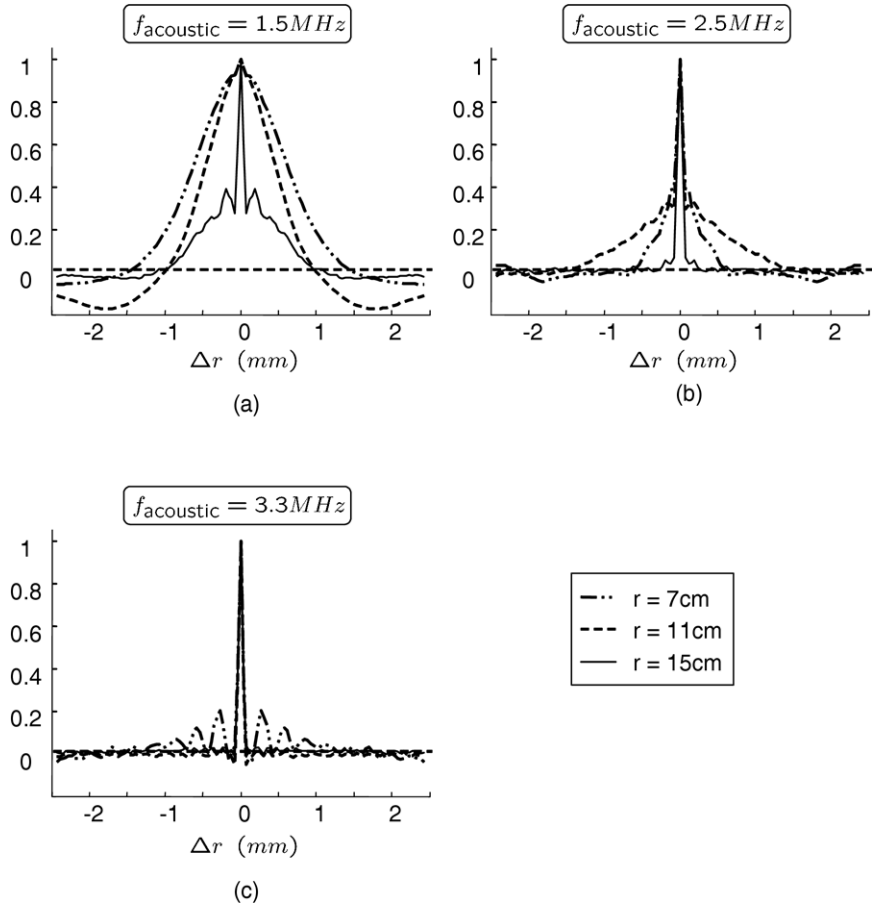

Fig. 11. Radial normalized auto-correlation at different radial distances, for various AFs. The correlation width tends to get narrower with radial distance.

$$r_{\text{equilibrium}} = \frac{1}{\alpha_{\text{high}}} \ln\left(\frac{2}{1 + e^{-\alpha_{\text{high}} R_{\max}}}\right). \tag{16}$$

Compounding K frequencies

In general, when compounding K images, it is possible to divide the radial axis into $K - 1$ consecutive segments at the most, as in Fig. 5. The k^{th} segment is $r \in [R_k^{\min}, R_k^{\max}]$, where

$$R_1^{\min} = 0$$

$$R_{K-1}^{\max} = R^{\max}$$

$$R_{k-1}^{\max} = R_k^{\min}, \ k = 1, \ldots, K-1. \tag{17}$$

We arrange the input images in descending order of AF. Then, in each segment, only a pair of raw frames are used, according to their AF: starting with the high resolution images (high AFs) near the probe, and finishing with images having high signal to system-noise ratio (lower AFs) far from the probe. In each segment, depth-dependent averaging of the image pair is done. In the first segment, we average the first and second images, in the second segment we average the second and third images, etc. Based on the example in eqn 15, the weights may be

$$\omega_{\text{high}}(r) = \frac{e^{-\alpha_{\text{high}}(k) r} - e^{-\alpha_{\text{high}}(k) R_{\max}(k)}}{e^{-\alpha_{\text{high}}(k) R_{\min}(k)} - e^{-\alpha_{\text{high}}(k) R_{\max}(k)}}, \ k = 1, \ldots, K-1, \tag{18}$$

The transition between segments is seamless. The reason is that a frame that is used in consecutive segments is weighted continuously across segments, while the other frames have a zero weight in the segment-seam.

Here the main degrees of freedom are the transition depths $\{R_k^{\max}\}_{k=1}^{K-1}$. Given them, the choise of $r_{\text{equilibrium}}$ and α_{high} is not critical. How are the transition depths chosen? One option is to let the physician choose them. Another option is to pre-set them according to empirical experience, and allow the operator/physician to fine tune the settings. We chose $\{R_k^{\max}\}_{k=1}^{K-1}$ according to our experience. Yet, since this matter depends on the inspected tissue, it deserves further research.

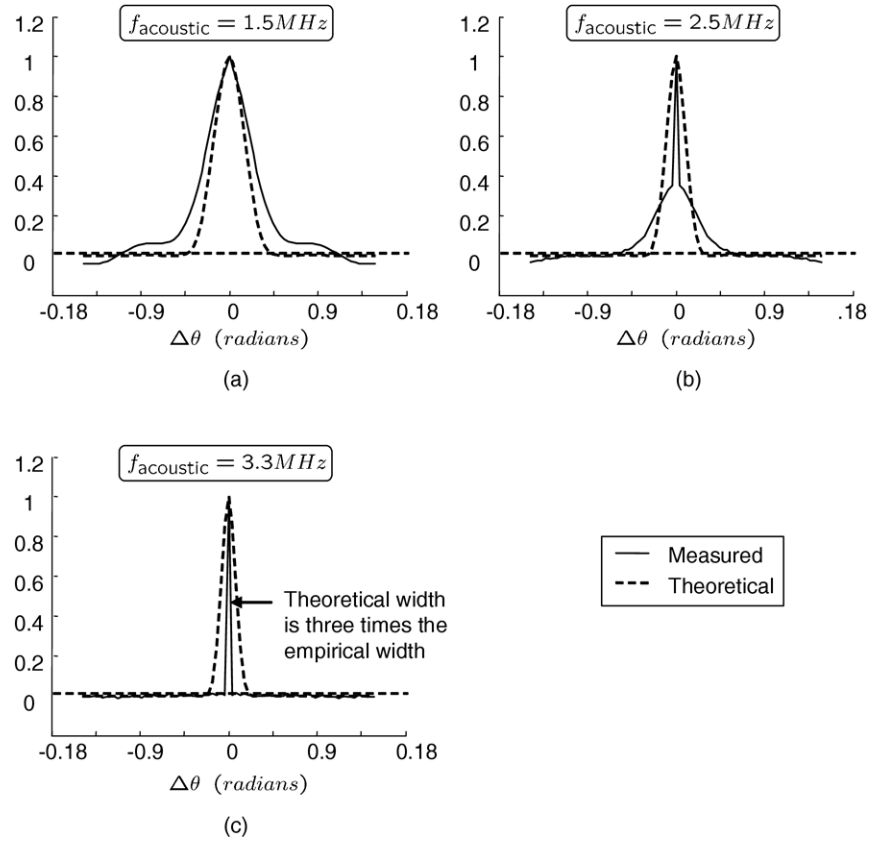

Fig. 12. Theoretical lateral normalized auto-correlation, compared to the measured one, for various AFs, at $r = 11$ *cm.* Existing models for lateral auto-correlation are consistent with measurements only at low AFs (a).

Stochastic reconstruction

The depth-dependent averaging method described in previous section implicitly assumes that noise is uncorrelated. Furthermore, that method is point-wise, thus, adjacent pixels are not exploited. In this section we seek a different method, that alleviates this assumption. It exploits the noise correlation functions, whose characteristics are described later in Sec. Empirical Noise Statistics. The method is spatially varying, based on the best linear unbiased estimator (BLUE), also known as Gauss-Markov or weighted least squares (Kay 1993). Our stochastic reconstruction is based on the following principles

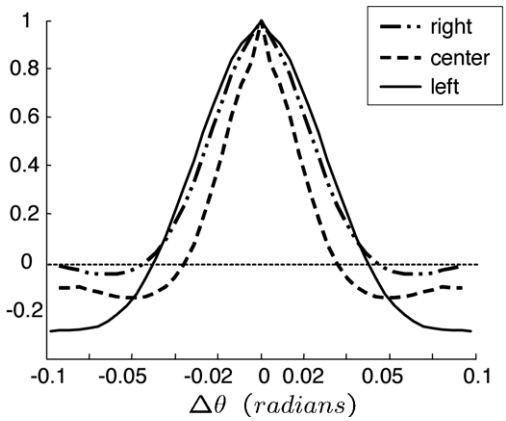

Fig. 13. Lateral auto-correlation in different lateral distances from the main axis. It is reasonable to assume that the auto-correlation is laterally invariant.

- The compounding should be space (depth) variant, since the statistics of noise changes with the depth *r,* as the PSF.
- In speckles, adjacent pixels are correlated (Wagner et al. 1983). Therefore, it is desirable that the compounding will not be pointwise. On the contrary, it should account for this spatial correlation.
- Speckles are correlated when acquired with different AFs (Walker and Trahey 1998). Therefore, simple averaging is not very efficient for speckle reduction. Instead, compounding needs to account for the cross-correlation between images taken in different AFs.
- The method is not intended for sharpening. Therefore, it does not include de-blurring. Nevertheless, we do not want to further blur existing information.

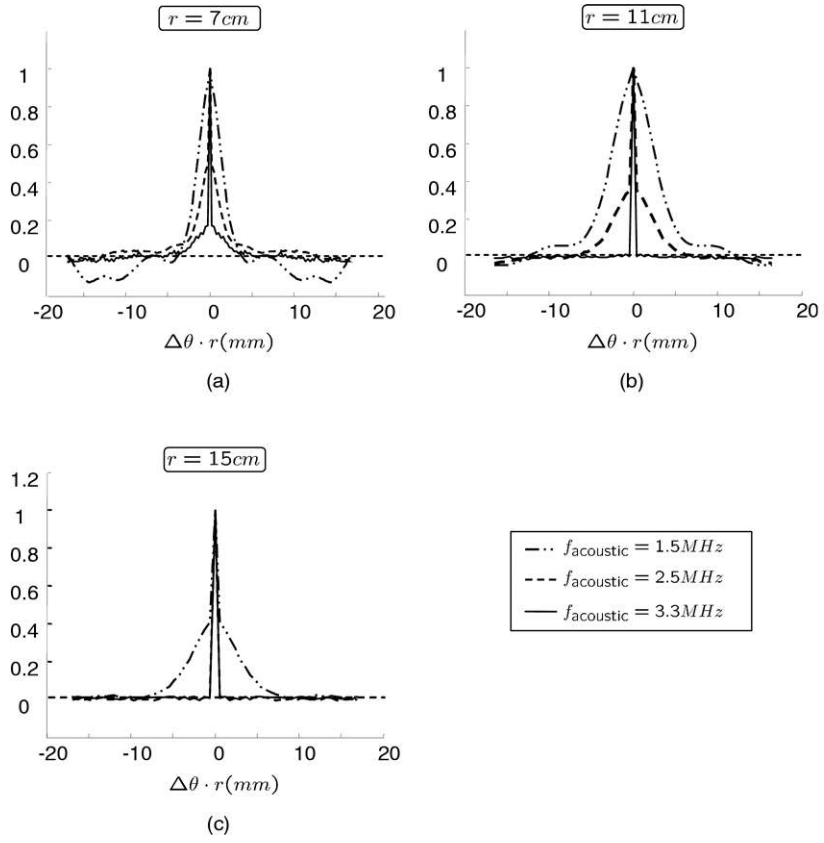

Fig. 14. Lateral normalized auto-correlation at different AFs, at various radial distances. The higher the AF is, the narrower the auto-correlation function is. This represents an image with higher resolution in the lateral direction, along with more dominant system noise.

In the following we detail our solution.

Matrix formulation

From now on, we refer to the signals $\mathrm{a}^{\mathrm{magnitude}}$ and $\mathrm{a}^{\log}$ as discrete $N \times 1$ vectors. Let us acquire K images in different AFs. Based on eqn 6,

$$\begin{pmatrix} \mathrm{a}_1^{\log} \\ \mathrm{a}_2^{\log} \\ \vdots \\ \mathrm{a}_K^{\log} \end{pmatrix} = \begin{pmatrix} \log \mathrm{a}_1^{\mathrm{magnitude}} \\ \log \mathrm{a}_2^{\mathrm{magnitude}} \\ \vdots \\ \log \mathrm{a}_K^{\mathrm{magnitude}} \end{pmatrix} + \begin{pmatrix} \mathrm{s}_1^{\log} \\ \mathrm{s}_2^{\log} \\ \vdots \\ \mathrm{s}_K^{\log} \end{pmatrix}. \tag{19}$$

At this point, we use the principle mentioned above, of not attempting to invert blur. Thus, we do not consider the blur h when we reconstruct the object (in the discussion and summary section we discuss a de-blurring option). Rather, we use a δ function for h in eqn 2. This yields $\hat{a}_0(r,\theta) = e^{2\alpha r\, f_{\mathrm{acoustic}}}\, a^{\mathrm{RF}}(r,\theta)$. Therefore, we set

$$a_k^{\mathrm{magnitude}} \approx \left|\mathrm{envelope}(\hat{a}_0)\right|, \tag{20}$$

for all k. Since all frames include a similar object content, we set

$$a_1^{\mathrm{magnitude}} \approx a_2^{\mathrm{magnitude}} \approx a_K^{\mathrm{magnitude}} \approx \cdots = a^{\mathrm{magnitude}}. \tag{21}$$

Nevertheless, each frame $\mathrm{a}_k^{\log}$ has different noise, especially speckle noise. Equation 19 then degenerates to

$$\begin{pmatrix} \mathrm{a}_1^{\log} \\ \mathrm{a}_2^{\log} \\ \vdots \\ \mathrm{a}_K^{\log} \end{pmatrix} = \begin{pmatrix} \mathrm{I} \\ \mathrm{I} \\ \vdots \\ \mathrm{I} \end{pmatrix} \log(\mathrm{a}^{\mathrm{magnitude}}) + \begin{pmatrix} \mathrm{s}_1^{\log} \\ \mathrm{s}_2^{\log} \\ \vdots \\ \mathrm{s}_K^{\log} \end{pmatrix}, \tag{22}$$

where I is the identity matrix.

BLUE

Consider data $\mathrm{a}^{\mathrm{data}}$ in the general linear model

$$\mathrm{a}^{\mathrm{data}} = \mathrm{Ha} + \mathrm{n}, \tag{23}$$

where H is a known $KN \times N$ matrix (operator), a is an $N \times 1$ vector of variables to be estimated, and **n** is an $N \times 1$ noise vector with zero mean and covariance C. The Gauss-Markov theorem (Kay 1993) states that the best linear unbiased estimator (BLUE) of a is

$$\hat{a} = (\mathrm{H}^T\mathrm{C}^{-1}\mathrm{H})^{-1}\mathrm{H}^T\mathrm{C}^{-1}\mathrm{a}^{\mathrm{data}}, \tag{24}$$

where T denotes transposition.

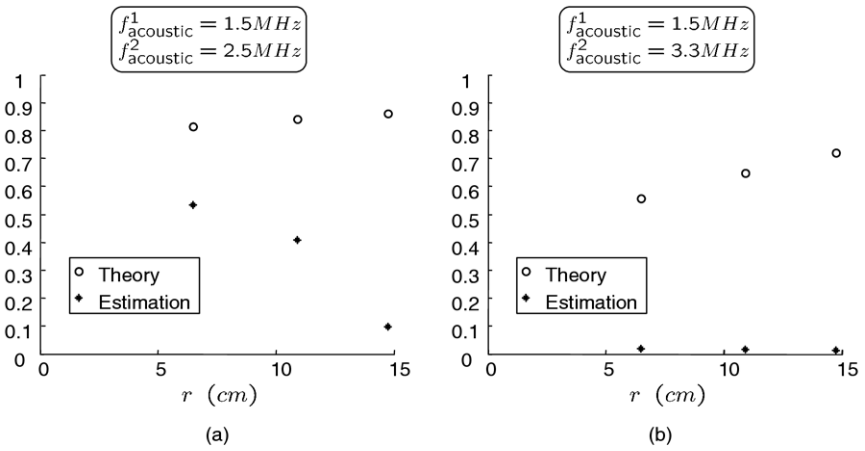

Fig. 15. Radial normalized cross-correlation model vs. empirical measurements. The model is higher than the measurements, and in an opposite trend. This phenomenon is more pronounced in high AFs.

Applying the BLUE on eqn 22 is possible. We substitute a = log ($a^{\text{magnitude}}$) in eqns 23 and 24, while a^{data} represents the vector on the left-hand-side of eqn 22. The noise covariance matrix C used in eqn 24 has the form

$$C = \begin{pmatrix} C_{s_1^{\log} s_2^{\log}} & C_{s_1^{\log} s_2^{\log}} & \cdots & C_{s_1^{\log} s_K^{\log}} \\ C_{s_2^{\log} s_1^{\log}} & C_{s_2^{\log} s_2^{\log}} & \cdots & C_{s_2^{\log} s_K^{\log}} \\ \vdots & & \ddots & \\ C_{s_k^{\log} s_1^{\log}} & C_{s_K^{\log} s_2^{\log}} & \cdots & C_{s_K^{\log} s_K^{\log}} \end{pmatrix}, \tag{25}$$

where $C_{s_k^{\log} s_i^{\log}}$ is the cross-covariance matrix between two speckle images $s_k^{\log}$ and $s_i^{\log}$ in different AFs. From eqn 24, we see that the BLUE performs a linear combination of all the data a^{data} (all pixels in all images) in order to estimate the value in each pixel of â. Therefore, the BLUE may potentially be extended to perform deconvolution (deblurring), in addition to noise-reducing averaging, or be used for noise whitening. Nevertheless, in our case

$$H = (I, I, \cdots, I)^T, \tag{26}$$

since we do not attempt deblurring. The BLUE exploits the correlation between variables. This enables denoising based on partially correlated variables. This is contrary to a simple average, which implicitly assumes uncorrelated variables.

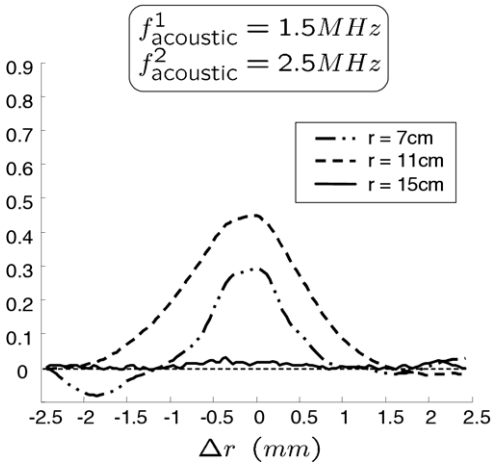

Fig. 16. Radial normalized cross-correlation at various radial distances. The signals lose cross-correlation at $r = 15$ *cm* due to a low SNR.

Spatially varying BLUE

To use the BLUE, we need to know the noise mean and covariance (*statistics*), in the set of raw frames we use. Let us first examine a certain block in the image. We can assume stationarity within this block. However, the statistics change in different image regions. Is there a need to divide the whole image to blocks, and measure the statistics within each of them? Practically, the answer is *no.* Since the statistics change gradually, it is possible to examine a few blocks in the field of view (FOV) as illustrated in the left side of Fig. 6, and measure the noise statistics only within them. This processing is applied in the polar coordinate domain, as illustrated in Fig. 6. Then, the speckle statistics around any point in the FOV can be deduced. The measurement of the statistics in these few selected blocks is described in Sec. Estimation of noise statistics. The BLUE uses the cross-correlation between different channels. As any cross-correlation function, it depends on the lag (Δr, $\Delta\theta$) between pixels. The size of the covariance matrix depends on the maximum lag in the radial direction and on the maximum lag in the lateral direction. Empirical measurements that we performed in several images showed a fast decrease in

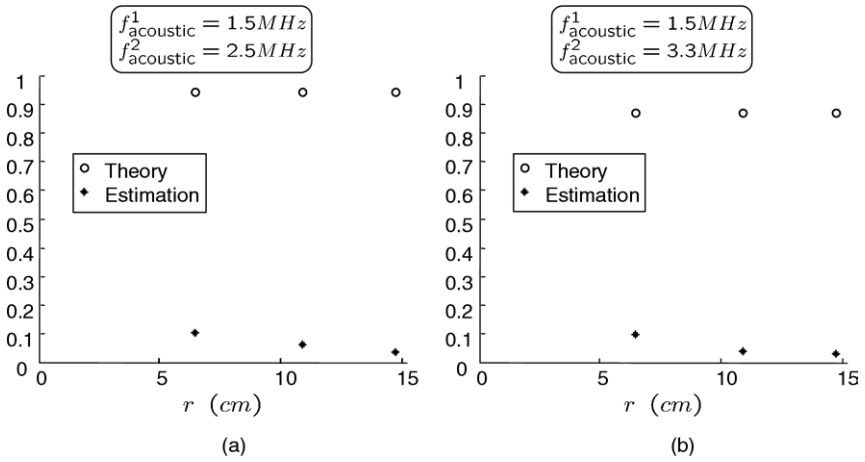

Fig. 17. Model of lateral cross-correlation vs. estimation. The model is higher than the estimation and is not depth-dependent.

the off-diagonal elements of the covariance matrix. We conclude that the lengths of the spatial correlation are short. Hence, small lags are sufficient to express the statistics. We are thus allowed to use small regions, for which the maximum Δr is $\approx$ 40 pixels corresponding to $\approx$ 1.5 *mm* in our system.

We now have the statistics in a few blocks. Then, using interpolation, we infer the statistics in any region centered on any pixel in the FOV. Subsequently, we can apply the BLUE around each pixel in the image. In other words, around each pixel, we define a small region, and since the noise statistics in this region has been estimated in the previous steps, we can apply the BLUE for this pixel.

RESULTS

Empirical noise statistics

The current models described in the Prior models for noise statistics section are not sufficiently accurate, since they do not take into account the spatial dependency of the statistics, and they assume system noise to be negligible. Here we empirically explore various correlation functions of the noise. A few words about the figures and terms used in this section. For display purposes, we plot the normalized correlations, and all images are displayed in their *polar coordinates.* Hence, pixels in each row are in the same depth, and pixels in any specific column are in the same lateral angle. When using the term *auto-correlation,* we refer to the auto-correlation between pixels in a single image (acquired with one AF), at different coordinates *e.g.* $\hat{R}_{s_k}(\Delta r)$ $\hat{R}_{s_k}(\Delta\theta)$. When using the term *cross-correlation,* we refer to pixels in different AFs (yet the same object), at different coordinates e.g. $\hat{R}_{s_k s_i}(\Delta r, \Delta\theta)$. In this section, we explore the auto-correlation and the cross-correlation both in the radial and lateral directions, as summarized in Table 1. The AFs used here are 1.5 *MHz,* 2.5 *MHz* and 3.3 *MHz.* They are referred to as the low, middle and high AFs, respectively. The various radial distances are illustrated in Fig. 7. The various lateral distances from the main axis are presented in Fig. 8.

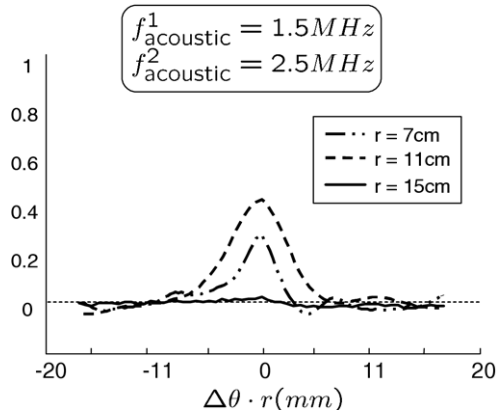

Fig. 18. Lateral cross-correlation. The cross-correlation is lost at $r = 15$ *cm,* due to low SNR.

Radial auto-correlation

Figure 9 compares the estimation $\hat{R}^{\text{radial}}_{s_k}(\Delta r)$ with the model of the radial auto-correlation (eqn 9), for a low AF image, at different radial distances *r.* At $r = 7$ *cm,* the model is similar to the empirical data. At $r = 11$ *cm,* $\hat{R}^{\text{radial}}_{s_k}(\Delta r)$ is wider than predicted by the model. This can be explained by a bandwidth decrease due to attenuation, which is stronger than in the model: a smaller bandwidth broadens the radial PSF, which in turn increases the correlation range of speckles. In contrast, at $r = 15$ *cm,* $\hat{R}^{\text{radial}}_{s_k}(\Delta r)$ is much narrower than the theoretical $R^{\text{radial}}_{s_k}(\Delta r)$, due to the dominant system noise.

Figure 10 plots the results for the high AF image, at

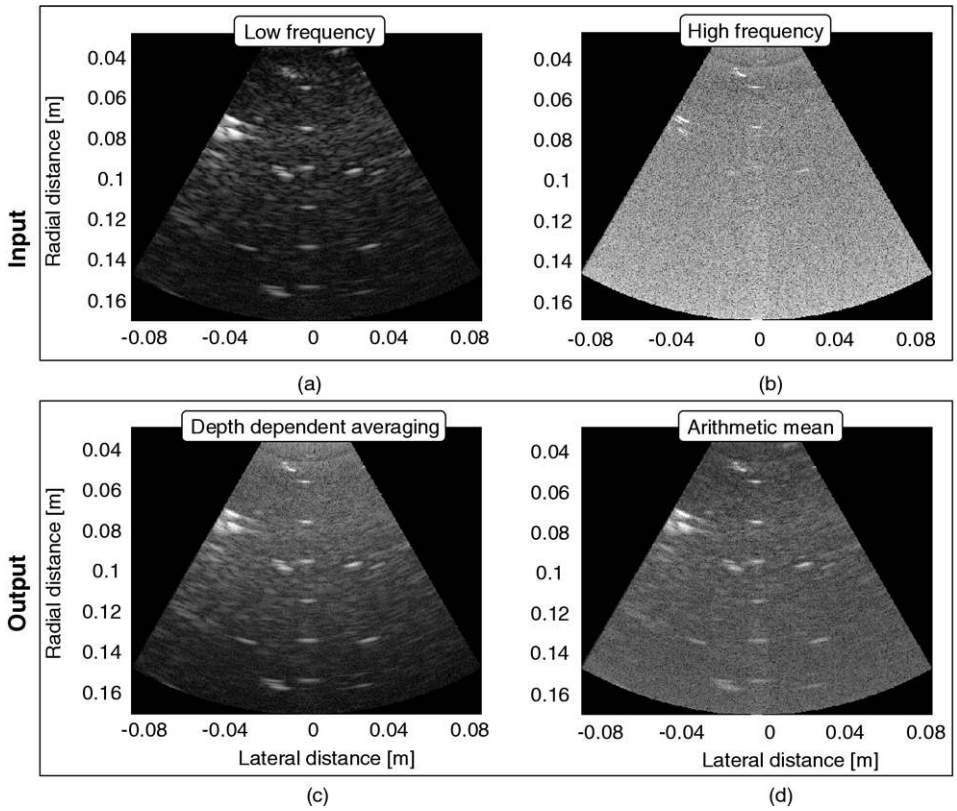

Fig. 19. (a) and (b) Input images. (c) Result of depth-dependent averaging. (d) Result of arithmetic mean of the two frames.

different radial distances. At all distances, $\hat{R}_{s_k}^{\text{radial}}(\Delta r)$ is much narrower than $R_{s_k}^{\text{radial}}(\Delta r)$, and it resembles a delta function. Hence, system noise is dominant in all distances. From these plots, we conclude that the existing model for $R_{s_k}^{\text{radial}}(\Delta r)$ is accurate mainly at short distances and low AFs.

Now, we further explore $\hat{R}_{s_k}^{\text{radial}}(\Delta r)$. Figure 11 compares it at different radial distances for various AFs. It is symmetric, as excepted, and its width depends on the radial distance r. We note again that at $r = 11$ *cm,* $\hat{R}_{s_k}^{\text{radial}}(\Delta r)$ is wider than at 7 *cm.* Far from the probe ($r = 15$ *cm*), the auto-correlation for all AFs becomes very narrow. This is typical for white noise, associated with system noise, which dominates the signal in that depth. Another way to look at it is that, the higher the AF, the narrower the auto-correlation function. This represents an image with higher radial resolution, along with more dominant system noise.

Lateral auto-correlation

Figure 12 compares the estimation $\hat{R}_{s_k}^{\text{lateral}}(\Delta\theta)$ with the model of the lateral auto-correlation $R_{s_k}^{\text{lateral}}(\Delta\theta)$. The plots present the results at $r = 11cm,$ for different AFs. Note that the variance of $\hat{R}_{s_k}^{\text{lateral}}(\Delta\theta)$ decreases with the AF, and theoretically $R_{s_k}^{\text{lateral}}(\Delta\theta)$ narrows with the AF as well. Yet, $\hat{R}_{s_k}^{\text{lateral}}(\Delta\theta)$ narrows faster. This may be caused by the increased dominance of system noise, which is not accounted for in the theoretical model of eqn 9. As in the radial case, we conclude that existing models for lateral auto-correlation are accurate mainly at low AFs. We now study further $\hat{R}_{s_k}^{\text{lateral}}(\Delta\theta)$. Figure 13 shows that $\hat{R}_{s_k}^{\text{lateral}}(\Delta\theta)$ is rather insensitive to the lateral position. Hence, it is reasonable to assume that the auto-correlation is practically laterally invariant. Figure 14 compares the lateral auto-correlation when using different AFs. The functions $\hat{R}_{s_k}^{\text{lateral}}(\Delta\theta)$ at $r = 11$ *cm* is wider than the one at $r = 7$ *cm,* since we are out of focus at $r = 11$ *cm.* Generally, the width of the auto-correlation depends on the AF. The higher the AF, the narrower $\hat{R}_{s_k}^{\text{lateral}}(\Delta\theta)$ is, which represents an image with higher resolution in the lateral direction, along with more dominant system noise.

Cross-correlation

In the radial auto-correlation and lateral auto-correlation section, we explored the correlation within a single image. In this section, we look at the correlation coeffi-

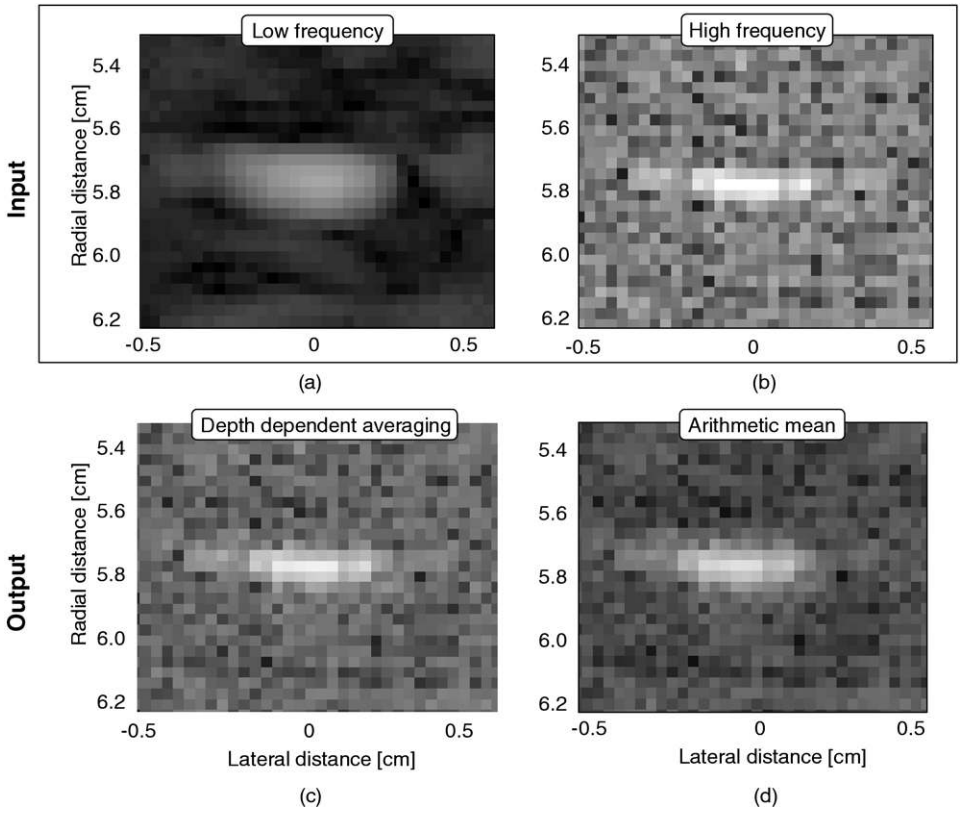

Fig. 20. Zoom on a scatterer near the probe, extracted from Fig. 19. Both depth-dependent averaging (c) and arithmetic mean (d) preserve the high resolution of the high AF image (b).

cient between different images of the same object $\rho_{s_k s_i}(\Delta r,\Delta\theta)$ and $\hat{\rho}_{s_k s_i}(\Delta r,\Delta\theta)$ [normalized $R_{s_k s_i}(\Delta r,\Delta\theta)$ and $\hat{R}_{s_k s_i}(\Delta r,\Delta\theta)$, respectively]. Note that the theoretical model in the prior models for noise statistics section is limited to corresponding pixels in two different images of the same object ($\Delta r = \Delta\theta = 0$). Our empirical study includes $\Delta r \neq 0$ as well. Figure 15 compares the estimation $\hat{\rho}^{\text{radial}}_{s_k s_i}(\Delta r)$ vs. the model of the cross-correlation coefficient value as in eqn 10, at different radial distances *r*. The function $\rho^{\text{radial}}_{s_k s_i}(\Delta r = 0)$ is much higher than $\hat{\rho}^{\text{radial}}_{s_k s_i}(\Delta r)$. Moreover, $\rho^{\text{radial}}_{s_k s_i}(\Delta r = 0)$ *increases* with *r,* due to attenuation-driven bandwidth decrease (detailed in the image formation section). In contrast, practically $\hat{\rho}^{\text{radial}}_{s_k s_i}(\Delta r)$ *decreases* with *r,* due to an increased dominance of the system noise. This phenomenon is more pronounced in high AFs. From these plots, we conclude that existing models for radial cross-correlation do not describe well the empirical data in the radial distances and AFs used in our estimations.

Figure 16 compares $\hat{\rho}^{\text{radial}}_{s_k s_i}(\Delta r)$ in the low and middle AFs. At $r = 7$ *cm* (where the SNR is high), both signals are correlated. The same applies to $r = 11$ *cm.* At $r = 15$ *cm* (where the SNR is low) $\hat{\rho}^{\text{radial}}_{s_k s_i}(\Delta r)$ is practically zero.

Similar conclusions are observed regarding $\hat{\rho}^{\text{lateral}}_{s_k s_i}(\Delta\theta)$. Figure 17 compares the estimation $\hat{\rho}^{\text{lateral}}_{s_k s_i}(\Delta\theta)$ with the model of the *lateral* cross-correlation at different radial distances. As for $\hat{\rho}^{\text{radial}}_{s_k s_i}(\Delta r)$, it can be noticed that the theoretical cross-correlation is higher than the estimation. The function $\rho^{\text{lateral}}_{s_k s_i}(\Delta\theta)$ does not change with the radial distance, although $\hat{\rho}^{\text{lateral}}_{s_k s_i}(\Delta\theta)$ decreases with depth, due to a more dominant system noise. Figure 18 compares the lateral cross-correlation at different AFs. It is generally significant at short lags. However, at $r = 15$ *cm* (where the SNR is low), $\hat{\rho}^{\text{lateral}}_{s_k s_i}(\Delta\theta)$ is practically zero. This phenomenon is more pronounced when using higher AFs.

From the empirical results presented above, we conclude that current models are inaccurate for large radial distances and/or high AFs. Thus, until accurate models are developed, correlation functions should be estimated from the data empirically if they are to be used effectively in recovery methods as the one described in Stochastic reconstruction section. Anyway, they vary with *r,* and the AF, but they are rather insensitive to θ.

Depth-dependent averaging

Depth-dependent averaging was applied to an image pair shown in Fig. 19. One image was acquired with

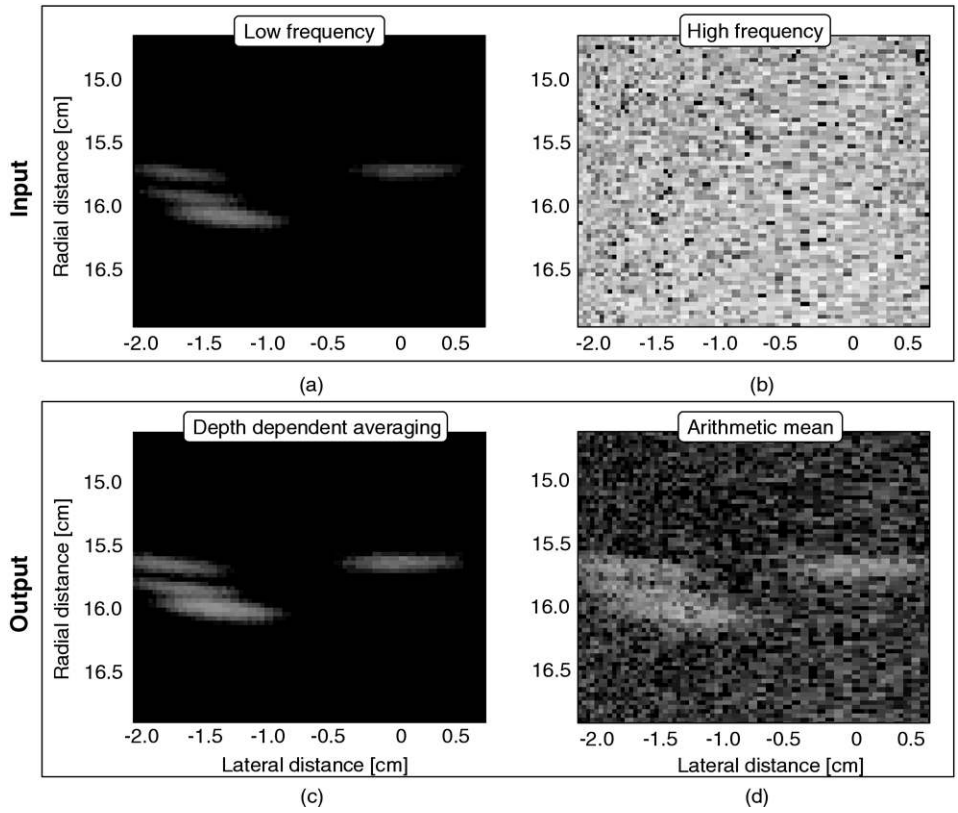

Fig. 21. Zoom on a scatterer far from the probe, extracted from Fig. 19. The three scatterers are hardly distinguished in the arithmetic mean image (d) contrary to depth-dependent averaging (c).

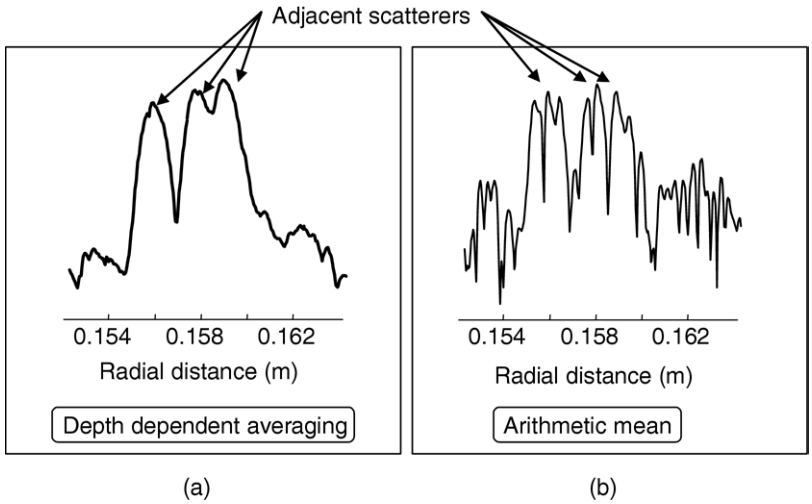

Fig. 22. A radial profile across three adjacent scatterers, extracted from Fig. 21. (a) The depth-dependent averaging distinguishes between adjacent scatterers. (b) The arithmetic mean hardly distinguishes between adjacent scatterers due to noise.

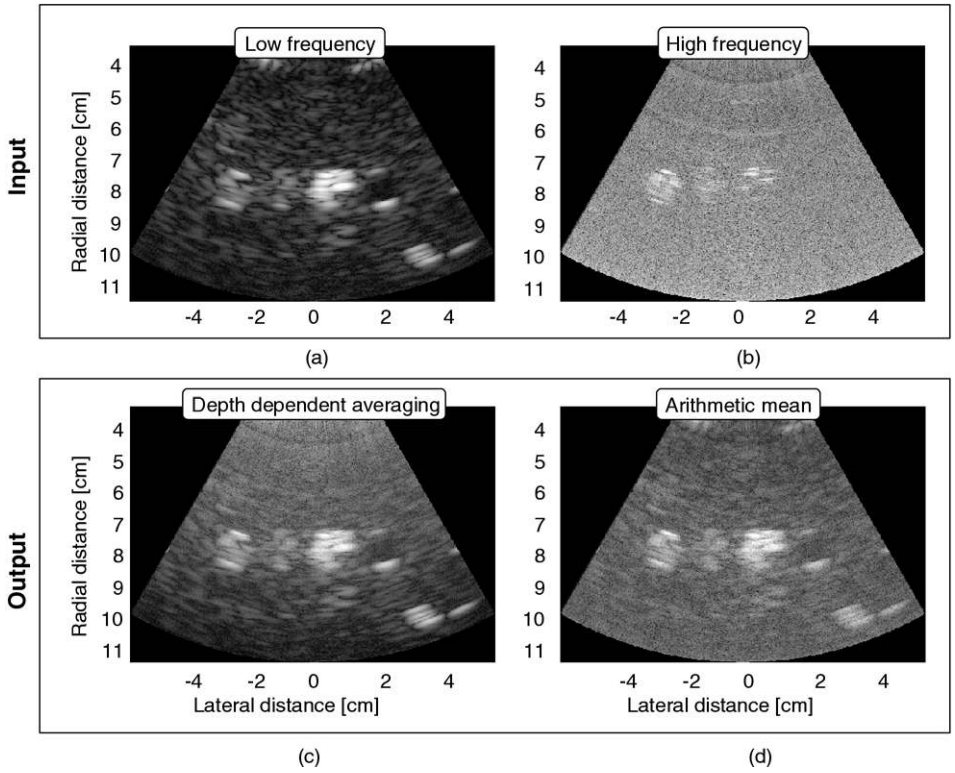

Fig. 23. (a) and (b) Input images. (c) Result of depth-dependent averaging. (d) Result of arithmetic mean.

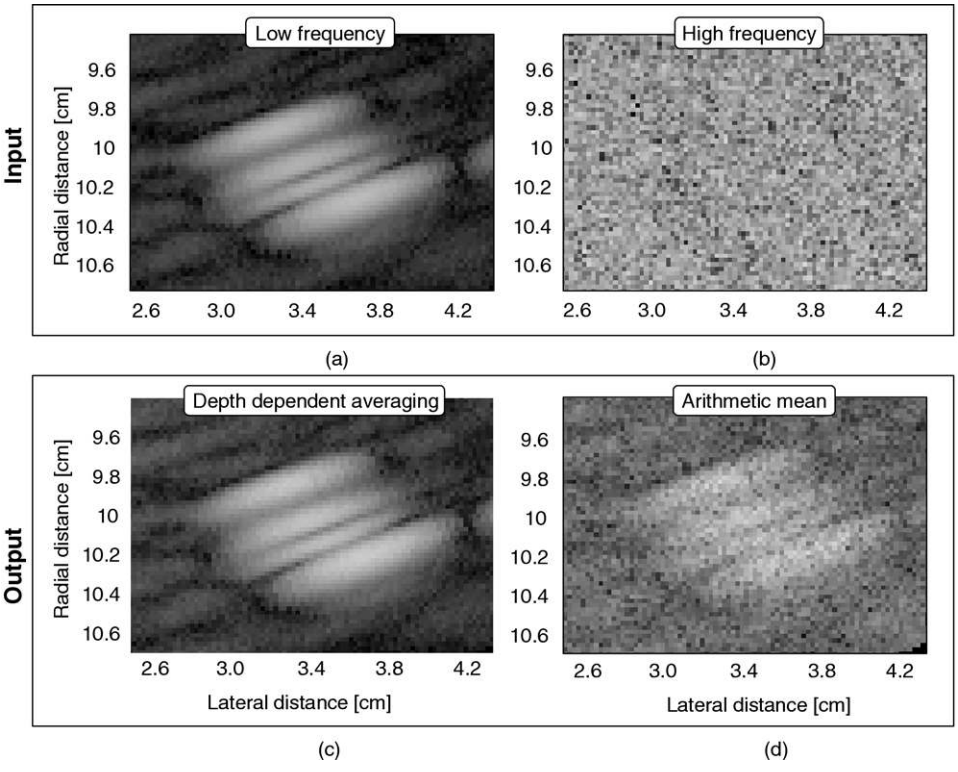

Fig. 24. Zoom on the scatterers far from the probe, extracted from Fig. 23. Depth-dependent averaging (c) distinguishes between them more clearly than arithmetic mean (d).

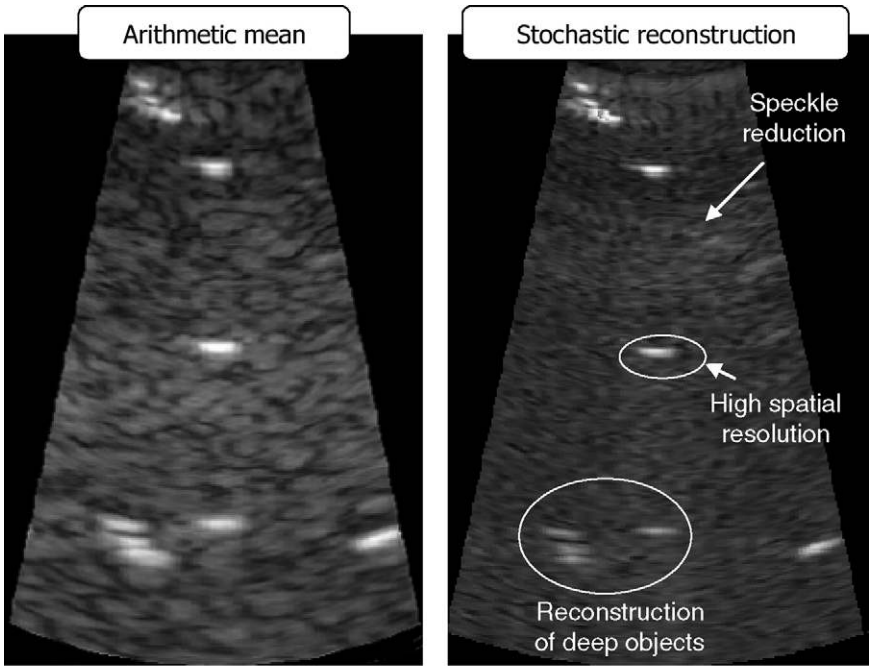

Fig. 25. Stochastic reconstruction (b) vs. simple averaging (a), based on the frames shown in Fig. 1. Stochastic reconstruction demonstrates reduced speckles, high spatial resolution and reconstruction of deep objects.

AF of 1.6 *MHz* (referred to as a low AF image). The second image was acquired with AF of 3.3 *MHz* (referred to as a high AF image). The weights used follow Equation 15 with $r_{\text{equilibrium}} = 6.8$ *cm*. We used $\{a_k^{\log}\}_{k=1}^2$ as input. The result is compared with an arithmetic mean of $\{a_k^{\log}\}_{k=1}^2$ in Fig. 19. In Figure 20 we zoom on a scatterer that is nearest to the probe. In this case, both methods preserve the high resolution of the high AF image. Nevertheless, there is a difference in the long range. In Fig. 21, we zoom on a scatterer, that is furthest from the probe, and the three adjacent scatterers on its left. Figure 22 plots a radial profile in these resulting images, corresponding to these three scatterers. It is difficult to distinguish between adjacent scatterers when looking at the arithmetic mean. However, the depth-dependent averaged image allows a clearer distinction of the scatterers. The same process was applied to another image pair, shown in Fig. 23. Figure 24 zooms on scatterers that are furthest from the probe. The arithmetic mean image is very noisy and it is difficult to distinguish between the scatterers, contrary to depth-dependent averaging.

Stochastic reconstruction

A raw image pair $\{a_k^{\log}\}_{k=1}^2$ is shown in Fig. 1. The low AF is 1.6 *MHz,* while the high AF is 3.3 *MHz*. The stochastic reconstruction was applied to the two images. The results are shown in Fig. 25. The speckle noise is significantly reduced, while high spatial resolution is maintained and deep objects are reconstructed. Figure 26 zooms on a region having three adjacent point targets, near the probe. The stochastic reconstruction reduces speckles around the scatterers, and the resolution is as in the high AF image. The peak signal to noise ratio (PSNR) of the two results is presented in Table 2. To estimate the PSNR, the signal is taken as the highest value of the scatterer and the noise value is taken as the standard deviation in the speckle area near that scatterer. Stochastic reconstruction yields a higher PSNR in all depths.

A similar process was applied to another image pair shown in Fig. 27. Here, the low AF is 1.6 *MHz* and the high AF is 2.6 *MHz*. The resolution of both input images is similar, and is maintained in the output. Nevertheless, the stochastic reconstruction reduces speckles without blurring of features.

DISCUSSION AND SUMMARY

We explored noise statistics in ultrasound images. Comparison of current statistical models with empirical data, indicates that there is some quantitative inconsistency. This occurs, we believe, since the models do not account for system noise, which is especially significant in large depths and high acoustic

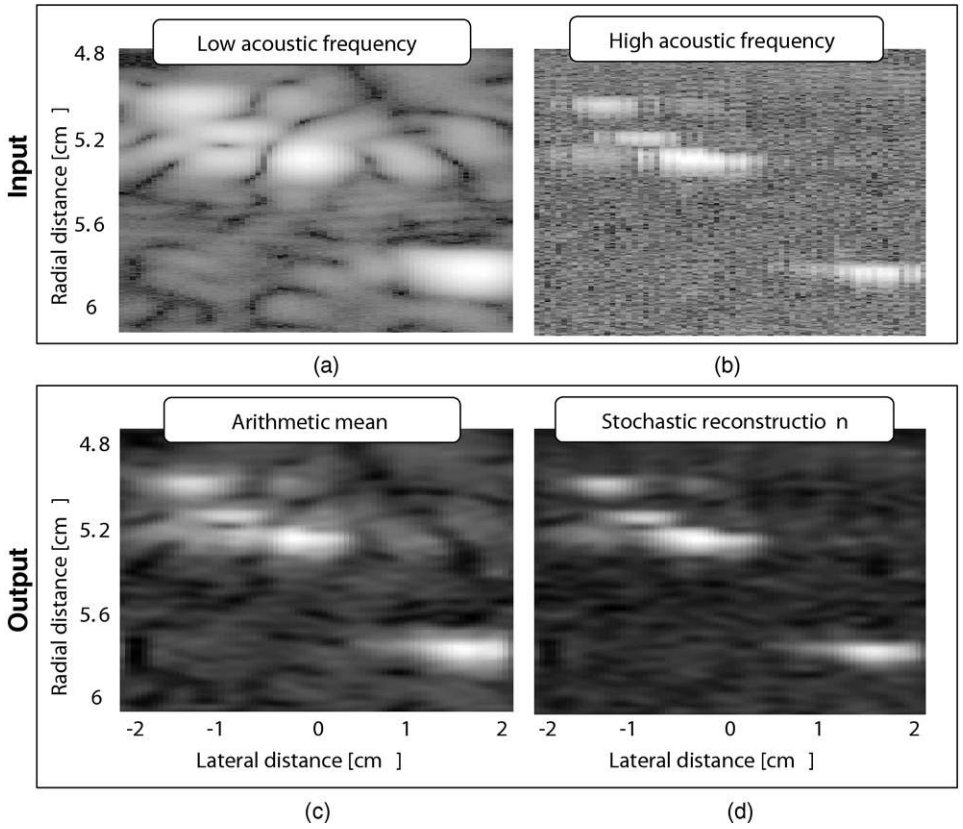

Fig. 26. Zoom on a section having point targets, extracted from Figs. 1 and 25.

frequencies. Also, we empirically looked at the auto-correlation and cross-correlation of images acquired towards frequency compounding. While we may assume that the covariance functions are insensitive to θ, they strongly depend on the depth r and on the AF. This is due to the relation between AF and resolution, as well as to the relation between AF, depth and attenuation. These empirical results along with the limited model of the cross-correlation to $\Delta r = \Delta\theta = 0$ suggest that there would be important benefits to new, revised theoretical analysis of ultrasound noise statistics. Such analysis needs to theoretically address both the spatial variations, and the combined effect of system and speckle noise.

Table 2. PSNR obtained by arithmetic mean and stochastic reconstruction in several depths.

Depth (cm)	Arithmetic mean	Stochastic reconstruction
6	66:1	117:1
7	72:1	133:1
8	48:1	73:1
9	61:1	83:1
10	78:1	124:1

We then considered frequency compounding. A prior compounding method is based on simple arithmetic mean, which is space invariant, and does not take into account the noise statistics. Thus, two new compounding methods were considered, which better account for the spatial variations of the source signals. These methods are depth-dependent averaging and stochastic reconstruction. Depth-dependent averaging is very simple to implement, and it can be performed on the fly, maintaining real time imaging. The stochastic algorithm is also depth-dependent. If the signals were uncorrelated, it would have been similar to the depth-dependent averaging. However, the stochastic method is more general, as it accounts for spatial and inter-frequency correlations. It thus enables further noise reduction.

Practical frequency compounding would rely on fast acquisition in two or more AFs. There exists enabling technology (Bouakaz et al. 2004; Forsberg et al. 2004; Xuecheng et al. 1998) allowing for that. Once this technology becomes mature, we believe that our algorithms can be used as a basis for exploiting frequency compounding. Future research can focus on the acquisition process as well as on the processing. In particular, it

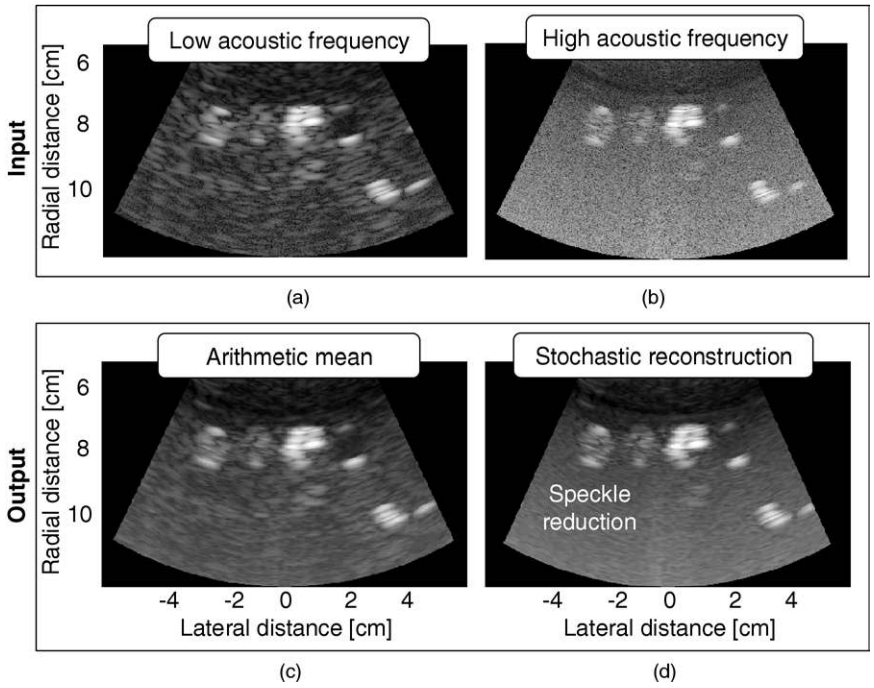

Fig. 27. Stochastic reconstruction vs. averaging for another image pair. Stochastic reconstruction (d) attenuates speckles, compared with an arithmetic mean (c).

is worth studying which AFs are optimal in this paradigm. We suggested de-blurring to be a complementary operation. Improved estimators may handle blur (perform deconvolution implicitly). Note that in this case, the theoretical model in eqn 23 involves a non-linear operation (eqn 3), which makes deconvolution more challenging.

Acknowledgments—This work was conducted while Yael Erez was at the Department of Electrical Engineering, Technion — Israel Institute of Technology. The authors thank Zvi Friedman and Yonina Eldar for useful discussions. Yoav Schechner is a Landau Fellow - supported by the Taub Foundation and an Alon Fellow. This research was partly supported by the Israel Science Foundation (Grant No. 315/04), by the Ministry of Industry and Trade, office of the Chief Scientist - "Magneton" Program and by the Technion VPR Fund for Research & Development. This continuous assistance is deeply appreciated. The research was carried out in the Ollendorff Minerva Center. Minerva is funded through the BMBF.

REFERENCES

Abd-Elmoniem KZ, Youssef AM, Kadah YM. Real-time specklerreduction and coherence enhancement in ultrasound imaging via nonlinear anisotropic diffusion. IEEE Trans on Biomed Eng 2002; 49:997–1014.

Amir I, Bilgutay NM, Newhouse VL. Analysis and comparison of some frequency compounding algorithms for the reduction of ultrasonic clutter. IEEE Trans Ultrason Ferroelectric Freq Control 1986;4:402–411.

Angelsen BAJ. Ultrasound imaging waves, signals, and signal processing, 1st ed. Trondheim, Norway: Emantec, 2000.

Aurich V, Weule J. Non-linear gaussian filters performing edge preserving diffusion. In: Sagerer G, Posch S, Kummert F, eds. Proceedings of the 17th DAGM Symposium. London, UK: Springer-Verlag, 1995:538–545.

Bouakaz A, Cate F, De Jong N. A new ultrasonic transducer for improved contrast nonlinear imaging. Phys Med Biol 2004;49: 3515–3525.

Burckhardt CB. Speckle in ultrasound b-mode scans. IEEE Trans Sonics Ultrasonics 1978;SU-25:1–6.

Busse LJ, Crimmins TR, Fienup JR. A model based approach to improve the performance of the geometric filtering speckle reduction algorithm. IEEE Ultrason Symp 1995:1353–1356.

Cincotti G, Loi G, Pappalardo M. Frequency decomposition and compounding of ultrasound medical images with wavelet packets. IEEE Trans Med Imaging 2001;20:764–771.

Dainty JC. Topics in applied physics, laser speckle and related phenomena. Springer-Verlag, Berlin. 1975.

Erez Y, Schechner YY, Adam D. Ultrasound image denoising by spatially varying frequency compounding. In: Franke K, Muller K-R, Nickolay B, Schafer R, eds. Proceedings of the DAGM-Symposium. Berlin, Germany: Springer-Verlag, 2006; 1–10.

Forsberg F, Shi WT, Jadidian B, Winder AA. Multi-frequency harmonic arrays: Initial experience with a novel transducer concept for nonlinear contrast imaging. Ultrasonics 2004;43:79–85.

Goodman JW. Statistical optics. New York: Wiley-Interscience, 1995.

Gupta S, Chauhan RC, Sexana SC. Wavelet-based statistical approach for speckle reduction in medical ultrasound images. Med Biol Eng Comput 2004;42:189–192.

Jain AK. Fundamentals of digital image processing, 1st ed. Engle-wood Cliffs, NJ: Prentice-Hall, 1989.

Kay SM. Fundamentals of statistical signal processing. Estimation theory. Englewood Cliffs, NJ: Prentice-Hall, 1993.

Kristoffersen K, Holm S, Saetre D. Mapping user interface controls to hardware. Vingmed Sound, 1998.

Loupas T, Mcdicken WN, Allan PL. An adaptive weighted median filter for speckle suppression in medical ultrasonic images. IEEE Trans Circuits Syst 1989;36:129–135.

Magnin PA, Von Ramm OT, Thurstone FL. Frequency compounding for speckle contrast reduction in phased array images. Ultraso Imaging 1982;4:267–281.

Meire HB, Farrant P. Basic Ultrasound. New York: John Wiley & Sons, 1995.

Oppenheim AV, Schafer RW. Digital signal processing, 1st ed. Englewood Cliffs, NJ: Prentice-Hall, 1975.

Papoulis A. Probability, Random Variables, and Stocahstic Processes, 2nd ed. Englewood Cliffs, NJ: Prentice-Hall, 1965.

Wagner RF, Smith SW, Sandrik JM, Lopez H. Statistics of speckle in ultrasound B-scans. IEEE Trans Sonics Ultrason 1983;30:156–163.

Walker WF, Trahey GE. The application of K-space in pulse echo ultrasound. IEEE Trans Ultrason, Ferroelect, Freq Control 1998; 45:541–558.

Webb S. The Physics of Medical Imaging. IOP publishing, Adam Hilger, Bristol. 1988.

Weickert J. A review of nonlinear diffusion filtering. Lect Notes Comput Sci 1997;1252:3–28.

Xuecheng J, Ladabaum I, Butrus TK. The microfabrication of capacitive ultrasonic transducers. J Microelectromech Syst 1998;7:295–302.